Title	Development of a low-mass and high-efficiency charged-particle detector
Author(s)	Naito, D.; Maeda, Y.; Kawasaki, N.; Masuda, T.; Nanjo, H.; Nomura, T.; Sasaki, M.; Sasao, N.; Seki, S.; Shiomi, K.; Tajima, Y.
Citation	Progress of Theoretical and Experimental Physics (2016), 2016(2)
Issue Date	2016-02
URL	http://hdl.handle.net/2433/227523
Right	© The Author(s) 2016. Published by Oxford University Press on behalf of the Physical Society of Japan.This is an Open Access article distributed under the terms of the Creative Commons Attribution License (http://creativecommons.org/licenses/by/4.0/), which permits unrestricted reuse, distribution, and reproduction in any medium, provided the original work is properly cited.
Type	Journal Article
Textversion	publisher

PTEP

Prog. Theor. Exp. Phys. **2016**, 023C01 (17 pages)
DOI: 10.1093/ptep/ptv191

Development of a low-mass and high-efficiency charged-particle detector

D. Naito[1,*], Y. Maeda[1,5], N. Kawasaki[1], T. Masuda[1,6], H. Nanjo[1], T. Nomura[2], M. Sasaki[3], N. Sasao[4], S. Seki[1], K. Shiomi[1,7], and Y. Tajima[3]

[1]*Department of Physics, Kyoto University, Kyoto 606-8502, Japan*
[2]*High Energy Accelerator Research Organization (KEK), Ibaraki 305-0801, Japan*
[3]*Department of Physics, Yamagata University, Yamagata 990-8560, Japan*
[4]*Research Core for Extreme Quantum World, Okayama University, Okayama 700-8530, Japan*
[5]*Present address: Kobayashi-Maskawa Institute, Nagoya University, Nagoya 464-8602, Japan*
[6]*Present address: Research Core for Extreme Quantum World, Okayama University, Okayama 700-8530, Japan*
[7]*Present address: Institute of Particle and Nuclear Studies, High Energy Accelerator Research Organization (KEK), Tsukuba, Ibaraki 305-0801, Japan*
*E-mail: d.naito@scphys.kyoto-u.ac.jp

Received April 24, 2015; Revised December 9, 2015; Accepted December 12, 2015; Published February 1, 2016

We have developed a low-mass and high-efficiency charged-particle detector for an experimental study of the rare decay $K_L \to \pi^0\nu\bar{\nu}$. The detector is important for suppressing the background with charged particles to the level below the signal branching ratio predicted by the Standard Model $\left(O\left(10^{-11}\right)\right)$. The detector consists of two layers of 3 mm thick plastic scintillators with embedded wavelength-shifting fibers and multi-pixel photon counters for the readout. We manufactured the counter and evaluated the performance in terms of light yield, timing resolution, and efficiency. With this design, we achieved an inefficiency per layer against penetrating charged particles of less than 1.5×10^{-5}, which satisfies the requirement of the KOTO experiment determined from simulation studies.

Subject Index C30, H10

1. Introduction

$K_L \to \pi^0\nu\bar{\nu}$ is a rare decay that directly violates CP symmetry. Its branching ratio is predicted with a small theoretical uncertainty to be $2.43(39)(6) \times 10^{-11}$ in the Standard Model (SM) of elementary particle physics [1], where the numbers in the first and second parentheses indicate parametric and intrinsic uncertainties, respectively. Several new physics models suggest large enhancement up to a few orders of magnitude in the branching ratio, and $K_L \to \pi^0\nu\bar{\nu}$ is a powerful tool for searching for new physics [2]. Experimentally, this decay has not yet been observed and an upper limit of 2.6×10^{-8} (90% CL) has been given (KEK-E391a [3]).

The KOTO experiment [4] is an experiment dedicated to observing the $K_L \to \pi^0\nu\bar{\nu}$ decay for the first time, using an intense kaon beam at the Japan Proton Accelerator Research Complex (J-PARC) [5]. We use an upgraded detector from KEK-E391a, which was the pilot experiment for the KOTO experiment. The KOTO experiment was designed to achieve a single event sensitivity of 8×10^{-12}.

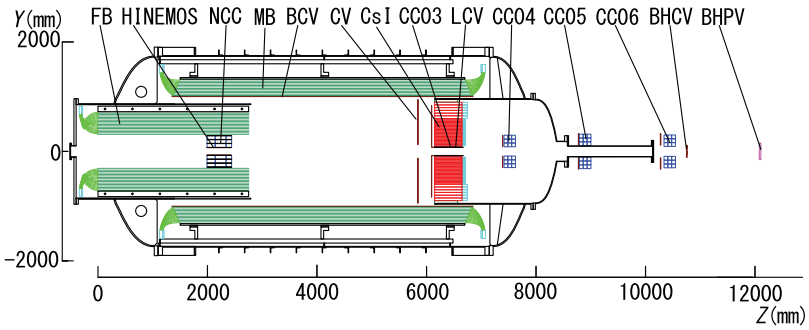

Fig. 1. Cross-sectional view of the KOTO detector. "CV" indicates the charged-particle counter that we have developed. Most of the detectors, including the CV, are installed in a cylindrical vacuum chamber. We search for the $K_L \to \pi^0\nu\bar{\nu}$ decay in flight that occurs in the central region of the vacuum chamber.

Figure 1 shows a schematic view of the KOTO detector. The signature of $K_L \to \pi^0\nu\bar{\nu}$ consists of two photons from a π^0 decay with no other particles detected. The position and energy of each of the two photons are measured by a CsI electromagnetic calorimeter. The decay-vertex position and the transverse momentum of π^0 are reconstructed to identify the decay. Hermetic neutral- and charged-particle detectors (veto detectors) surround the decay region in order to ensure that no extra particles exist. The hermetic detector system plays an essential role in achieving the background rejection factor of 10^{11} required for the experiment. The charged veto (CV) is located in front of the CsI electromagnetic calorimeter, and detects charged particles entering the calorimeter. Almost all the charged decay modes of K_L have two charged particles; if two charged particles fly toward the CsI calorimeter and are misidentified as two gammas, such an event can be a background event.[1] There are about 3×10^{10} times more K_L decays that include charged particles than the expected signal. The CV is required to reject such background events by more than a factor of 10^{10}, after other detectors are used to suppress the background. To achieve this goal, we installed two layers of plastic scintillators as the CV to cover the upstream surface of the calorimeter. The two charged particles from the K_L mainly make four hits on the two layers of the CV. Because the total reduction is expected to be the fourth power of the inefficiency of each layer, we can achieve the required background reduction if the charged-particle inefficiency is less than 10^{-3} for each layer. We have developed and evaluated a new detector for the CV to achieve the requirement.

2. CV design and production

2.1. Concepts

We used plastic scintillator strips with embedded wavelength-shifting (WLS) fibers for the CV. Strips of these scintillators are arranged to cover the whole region of the calorimeter. The segmentation is necessary to reduce the counting rate per readout channel.[2] It was designed with three functionalities: minimal interaction, small inefficiency, and good timing resolution.

[1] For the $K_L \to \pi^+\pi^-\pi^0$ decay, if π^- and π^+ have a charge exchange interaction $\left(\pi^- p \to \pi^0 n \text{ or } \pi^+ n \to \pi^0 p\right)$ before π^- or π^+ are detected by the CV, and particles in final states are not detected by any veto counters, $K_L \to \pi^+\pi^-\pi^0$ can be background events.

[2] From the simulation, the maximum hit rate of the scintillator strips is less than 250 kHz at the designed beam power of the KOTO experiment.

First, the low-mass feature is required to minimize neutron interaction at the CV for the following reason. At the neutral beam line for the KOTO experiment (the KL beam line), a small fraction of neutrons remains in the halo region of the beam. If a neutron interacts with the CV and generates a π^0 or η, two photons from the π^0 or η decay can fake a signal. To reduce such events, the mass of the CV must be as low as possible.

Second, small inefficiency is essential to achieve the KOTO goal. In other words, high light yield should be maintained, and there should be no gaps between the scintillator strips. The CV needs to have more than 10 photoelectrons (p.e.) per 100 keV energy deposit to achieve an inefficiency level of less than 10^{-3} at a 100 keV threshold,[3] according to our simulation study. If we reduce the thickness of the scintillator to suppress the interaction of the neutrons, the light yield decreases because the number of reflections increases and the light is attenuated at every reflection. This would increase the inefficiency. Using WLS fibers embedded in the plastic scintillators enabled the CV to reduce the effects of attenuation. The fibers absorb blue light ($\sim$430 nm) from the scintillator and emit green light ($\sim$480 nm), which is expected to have a longer attenuation length. The light from the fibers is read at both ends by multi-pixel photon counters (MPPCs). MPPCs have an approximately 2.5 times higher detection efficiency for green light ($\sim$45% at 480 nm [6]) than ordinary photomultipliers. The arrangement of the scintillator strips without gaps is important to minimize the inefficiency, which will be discussed later.

Third, the CV is required to have good timing resolution. Poor timing resolution requires a wider timing window to keep a sufficient efficiency, and causes event loss due to accidental hits. The timing resolution is required to be less than 3 ns to suppress the event loss to lower than 5%.

2.2. CV structure

The CV consists of two layers of plastic scintillators. Each layer is named "front" and "rear" along the beam direction. Figure 2 shows a schematic view of the CV layer.

Each layer has a quadrant structure with a 90° symmetrical arrangement, with a beam hole in the center. Each quadrant consists of twelve (eleven) scintillator strips in the front (rear) layer. Each scintillator is 70.7 mm wide and 3 mm thick. The lengths of the strips are determined so as to make the outer shape an octagon, as summarized in Table 1. The strips in a layer are tied onto a 0.8 mm thick carbon-fiber-reinforced-plastic (CFRP) plate with fluorocarbon wires passing through the cutouts in the edges of the strips. The cutouts of the neighboring scintillator strips overlap and make a 0.6 mm $\times$ 0.4 mm insensitive region. The ratio of the inefficient area to the whole area is 10^{-5} for all the cutouts, and is smaller than the inefficiency requirement ($<10^{-3}$). In order to minimize gaps between strips, the four sides of each strip are cut at an angle of 60°, as shown in Fig. 2, so that neighboring strips can be arranged with an overlap without increasing the thickness.

Each detector strip is composed of BC404 plastic scintillator, manufactured by Saint-Gobain [7], Y11 (350) WLS fiber by Kuraray [8], and S10943-0928(X) MPPCs by Hamamatsu Photonics [9]. Seven 1 mm diameter fibers are embedded and glued into grooves on each scintillator strip at 10 mm

[3] The 100 keV threshold enables the CV to detect charged pions that pass through the scintillator by more than 0.5 mm before a charge exchange interaction, with an inefficiency less than 10^{-4} [4]. A counting loss occurs when a charged pion undergoes the charge exchange interaction $\left(\pi^+ n \to \pi^0 p \text{ or } \pi^- p \to \pi^0 n\right)$ and gives a small energy deposit to the scintillator. This threshold is small enough to suppress the background from the $K_L \to \pi^+\pi^-\pi^0$ decay.

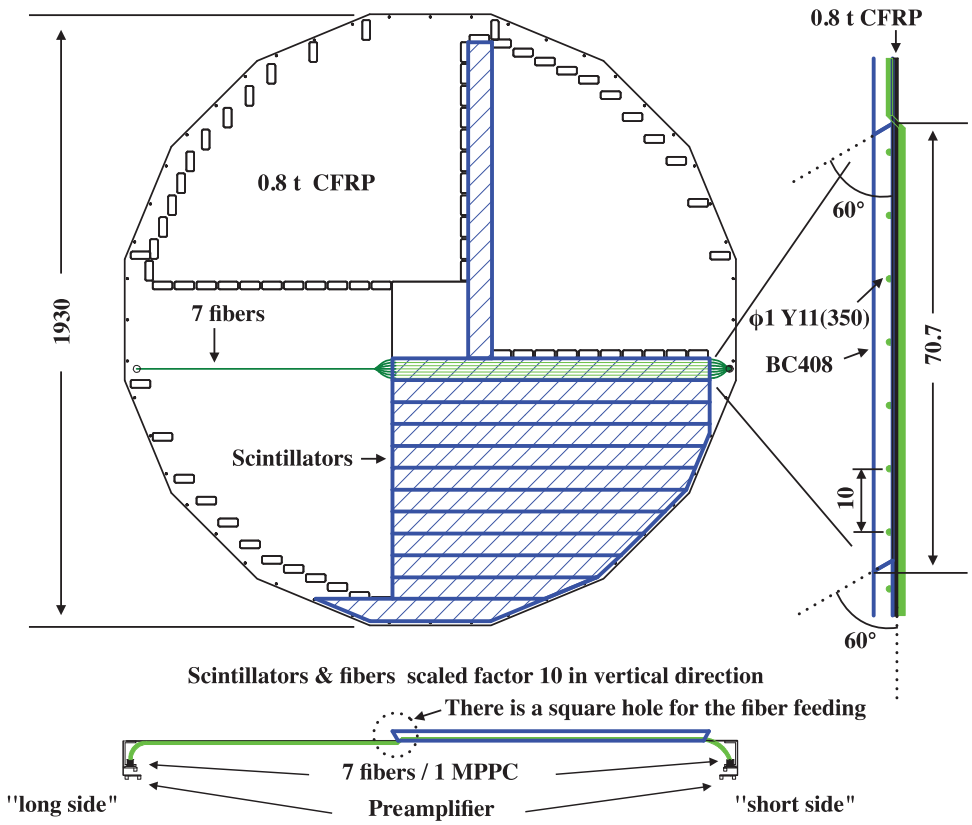

Fig. 2. Schematic view of a CV front layer. The figure at the bottom shows the side view of the scintillator near the center viewed from the bottom. We call the ends of a strip the "long side" and the "short side", according to the length of fibers extending out of the strip. In the bottom figure, the "long side" is the left side and the "short side" is the right side of the strip. The figure on the right shows a side view of the scintillator viewed from the right. Each layer has a quadrant structure with 90° symmetry. Plastic scintillator strips are tied onto an octagonal supporting CFRP plate with fluorocarbon wires passing through the cutouts in the edges of the strips. Rectangular holes on the CFRP plate are for routing WLS fibers to MPPCs at the outer circumference.

Table 1. Summary of the CV structure.

	Front layer	Rear layer
Outer radius (mm)	950	850
Beam hole size (mm × mm)	242 × 242	154 × 154
Number of scintillator strips	48 (12 × 4)	44 (11 × 4)
Length of the strips (mm)	644–1002	490–917
Number of readout channels	96	88

intervals. The cross section of a groove[4] is 1.1 mm × 1.1 mm. To achieve a readout at both ends without interfering with a neighboring quadrant, the fibers are not glued in the 20 mm region at the end of the strip and are fed to the opposite side of the CFRP plate through holes, as shown in Fig. 3. The fibers are bundled at both ends and connected to the MPPCs, which are mounted on the outer supporting structure. Each scintillator strip is wrapped with a reflector film: an aluminized polyester

[4] The bottom of the groove is a circular shape to make full contact between the surface of the fibers and the scintillator.

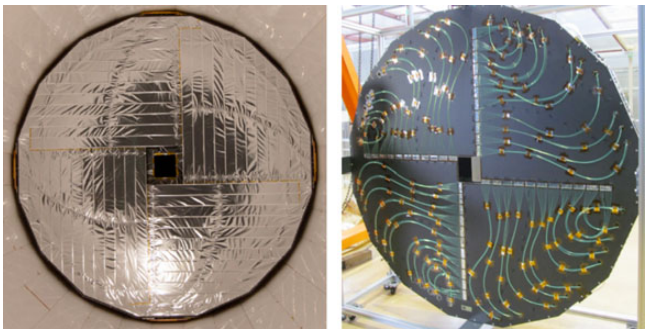

Fig. 3. Photographs of the CV layers. The left photograph shows an upstream view of the front layer. The scintillator strips are wrapped with aluminized mylar sheets. The right photograph shows a downstream view of the rear layer. The wavelength-shifting fibers, which come from the scintillators on the upstream side of the CFRP plate through the holes, are routed to MPPCs on the outer supporting ring.

Table 2. Summary of the MPPC specifications.

Effective photo-sensitive area	3 mm × 3 mm
Pixel pitch	50 μm
Number of pixels	3600
Number of channels	1ch
Package	Metal with TE cooler
Dark count (at 10°C)	200 kHz
Gain	8×10^5

film (Tetolight) manufacured by OIKE & Co., Ltd. [10]. The thicknesses of the base film and the deposited aluminum are 12 μm and 40–50 nm, respectively.

Table 2 shows the specifications of the MPPC. In order to stabilize the gain and quantum efficiency and reduce dark noise, a thermoelectric (TE) Peltier cooler is used to keep and control the temperature of the MPPCs at 10 ± 0.1 °C. For these purposes, we developed a 3 mm square MPPC, which is integrated with a Peltier device, jointly with Hamamatsu Photonics.

2.3. Production of the CV strip

The production of the scintillator strip had five steps: cutting a scintillator plate, cutting grooves, embedding fibers, bundling fibers at each end into a connector, and wrapping the strip with a reflector film. We first measured the thickness of sixteen raw scintillator plates over the whole area of 1010 mm × 570 mm by a laser displacement meter to determine how to cut strips out of the plates. The mean thickness was 3.10 mm and the standard deviation was 0.19 mm. The measurement accuracy was ±0.03 mm. Regions with thicknesses less than 2.75 mm were not used because the light yield under the grooves was too low and it would increase the inefficiency. After cutting strips out of the plates, we made seven grooves for fibers with a milling machine. Next, we embedded fibers into the grooves and glued them by using an automatic applicator of an optical cement (Eljen EJ-500 [11]). We then bundled the fibers at each end into a connector made with aluminum. The connector ensures optical coupling with the MPPC; it keeps the distance between the ends of the fibers and the surface of the MPPC at 0.6 mm.[5] The light loss at the coupling was estimated by a simulation to be 10% in

[5] There is a protective resin film (0.3 ± 0.2 mm in thickness) upon the surface of MPPC; we made the distance as short as possible.

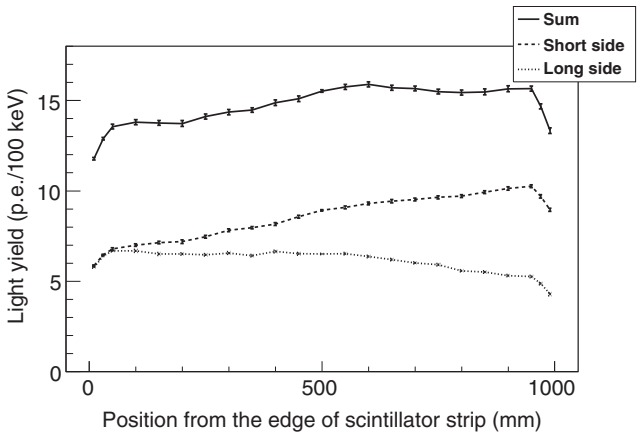

Fig. 4. Example of the light yield distribution as a function of the position of the ^{90}Sr β source. The horizontal axis indicates the distance of the source from the "long side" end of the strip. The configuration of "short side" and "long side" were mentioned in the caption of Fig. 2. The measured light yield was attenuated along the distance from the readout. The light yield was low in the regions where the fibers are not embedded in the scintillator.

the nominal case, 15% at most when a possible misalignment was considered. We glued the fibers to the connector with the optical cement and polished the end surface of the fiber bundle with a diamond polisher. Finally, we wrapped each scintillator strip with the reflector film, which was described in the previous section.

After the production of the strips, we checked their light yield by using a ^{90}Sr β source. Figure 4 shows the light yield of each scintillator strip as a function of the β source position. Here the light yields at both ends and the sum of the two are presented in units of the number of photoelectrons per 100 keV energy deposit. The energy deposit of the β ray was estimated by a simulation. We obtained the light yield of all the strips to be more than 10 p.e./100 keV in the whole region. For every group of four scintillator strips with the same shape and size in each layer (note that the CV has 90° symmetry), the light yields at the center of the strips matched with 2% in σ after correcting for thickness variations. We succeeded in the production of high-light-yield scintillator strips of good quality.

2.4. MPPC readout

Figure 5 shows the readout circuit for the MPPC. The anodes of MPPCs are connected to a common power supply, which determines the main bias voltage. The cathode of each MPPC is connected to a digital-to-analog converter (DAC) that adjusts the bias voltage individually. A signal from the MPPC cathode is sent to a 50-fold preamplifier through a 20 cm long coaxial cable. Table 3 summarizes the performances of the preamplifier. The signal, received via an AC coupling, is amplified by a 10-fold non-inverting amplifier and a 5-fold differential amplifier, and is sent to a 125 MHz analog-to-digital converter (ADC) module [12,13] through a shielded twisted pair (STP) cable. The ADC shapes a signal waveform by a 10-pole Bessel filter and records the pulse heights every 8 ns for 64 points (Fig. 6). In the KOTO experiment, the waveform information is used to resolve multiple pulses caused by high counting rates.

The combined gain of the MPPC and the preamplifier is monitored by checking the pulse height distribution for minimum ionizing particles (MIPs) passing through the CV layer. We also monitor the output charge distribution for one photoelectron gain. By evaluating the MIP peak in units of

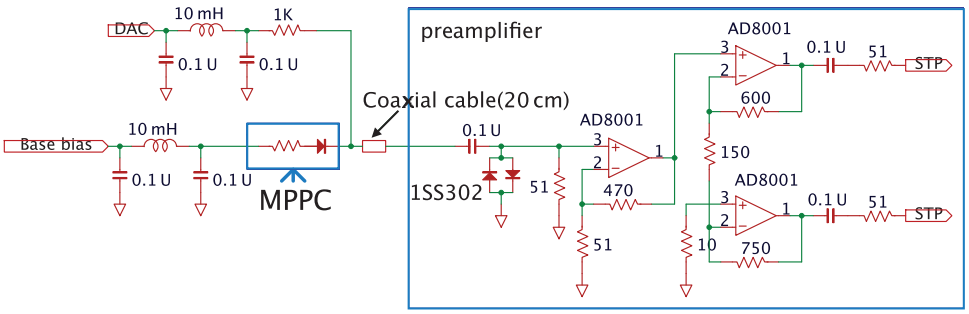

Fig. 5. Schematic of the MPPC bias and readout circuit. The left part indicates the MPPC and the bias voltage connection, and the right part indicates the preamplifier circuit.

Table 3. Summary of the performances of the MPPC preamplifier. These values were measured with a 51 Ω impedance.

Output dynamic range	2.5 V
Bandwidth	200 MHz
Gain	51
Power consumption	150 mW
Noise	2.4 mV (RMS)

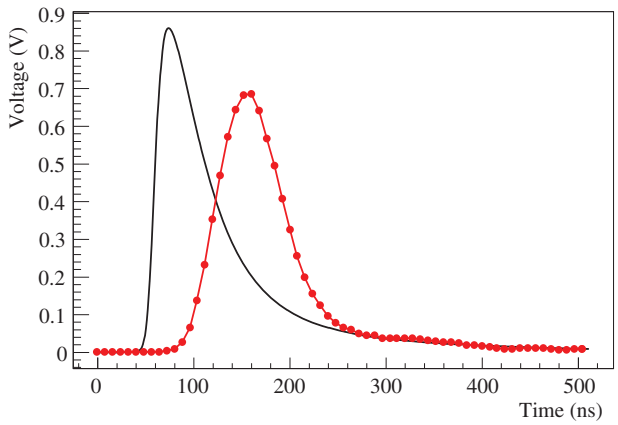

Fig. 6. Example of a CV pulse shape of charged particles. The smooth line shows the output of the preamplifier. The dots indicate data recorded by a 125 MHz ADC module, drawn with a poly-line through the data points. Both waveforms were obtained by averaging over 10 000 pulses.

photoelectrons, we monitor the light yield of the CV strip. It monitors both light output from the strip and the quantum efficiency of the MPPC.

3. Performance study of a prototype strip

Before the mass production of the CV strips, we evaluated the performance of a prototype strip by using a 600 MeV/c positron beam at the Research Center for Electron Photon Science (ELPH) at Tohoku University. Figure 7 shows the experimental setup for the study. Four plastic scintillators (T0, T3, T4, and T5[6]) were used to define the beam size (20 mm × 20 mm) and ensured that the

[6] To reduce the effect of the annihilation that occurs upstream of the CV, we prepared a thin (0.2 mm thick) plastic scintillator, T5, just in front of the CV. We can select charged particles with a small probability of an

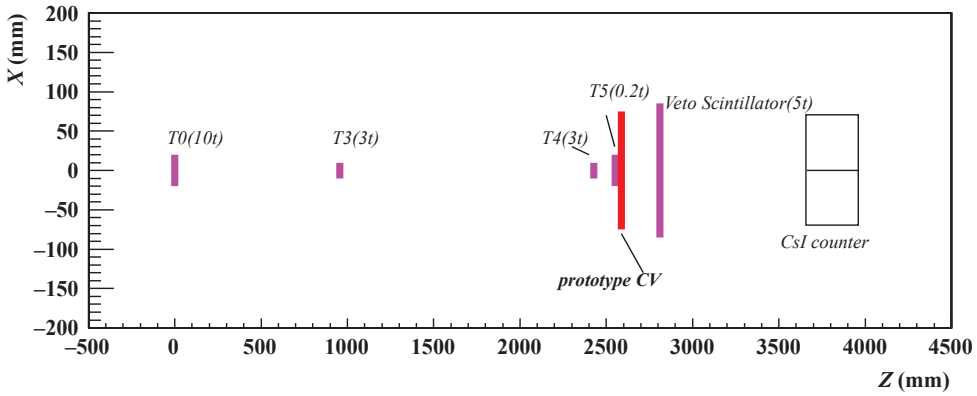

Fig. 7. Plan view of the setup for the performance study at ELPH at Tohoku University. Four plastic scintillators (T0, T3, T4, and T5) defined the positron beam, while another scintillator (veto scintillator) and an electromagnetic calorimeter (CsI counter) were located behind the prototype strip to identify annihilation events.

positrons were hitting the prototype strip. Another plastic scintillator (veto scintillator) and an electromagnetic calorimeter (CsI counter) were located downstream of the prototype CV to be tested, in order to identify positron annihilation events. We defined an event with energy deposits in the calorimeter without a hit in the veto scintillator as an annihilation event. The calorimeter was a 2×2 array of CsI crystals with dimensions of 7 cm square in cross section and 30 cm in length.

We used a 15 cm long and 7 cm wide prototype strip. In this study, we used a different readout system than the one described in Sect. 2.4, which includes a commercial amplifier module for the MPPC and a charge-integrating ADC for recording the signal.

Figure 8 shows the energy deposit distribution of the prototype. The result from our Monte Carlo (MC) simulation is also presented in the figure. According to the simulation study, energy deposits by MIPs peak around 0.5 MeV, and a feature in the region below 0.25 MeV has contributions from both the fluctuation due to the photoelectron statistics[7] and the effect of grooves for WLS fibers, where the effective scintillator thickness is thinner than in other places. The beam size defined with the plastic scintillators can contribute to the discrepancy between the data and the simulation around 0.25 MeV in Fig. 8, because it changes the contribution of the groove region. We defined the prototype strip as having had a hit if it has more than 100 keV energy deposit. Table 4 summarizes the results of the inefficiency measurement. Based on 41 events below the 100 keV threshold, the inefficiency of the prototype strip was determined to be 5.4×10^{-5}, which agreed well with the simulation result.

We investigated the events below 100 keV that were defined as inefficient events. Figure 9 shows the correlation between the energy deposits in the CsI counter and the veto scintillator. Among 41 events, seven events had energy deposits both in the CsI counter and the veto scintillator, and were categorized as the inefficiency for truly penetrating tracks due to the fluctuation of the photoelectron statistics.[8] The other 34 events had energy deposits only in the CsI counter, which means that only photons existed behind the prototype strip, and therefore were categorized as the inefficiency

annihilation inside T5. The contamination of the annihilation in T5 to the total annihilation events was 20%, based on a simulation.

[7] The light yield of the prototype strip was less than half of the achieved light yield in the production strips due to a bad optical connection between the WLS fibers and the MPPC.

[8] This type of inefficiency is expected to be small given the achieved light yield of the production strips.

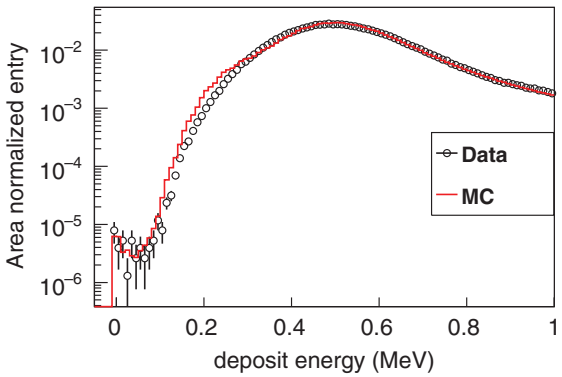

Fig. 8. Energy deposit in the prototype strip. The energy scale of the data was determined so that the peak values in the data and the simulation matched each other. The spectrum of the data was normalized to the area over a full energy range. The simulated spectrum was also normalized in the same way. The energy spectrum of the simulation was smeared with the measured light yield in this measurement (6.8 p.e./100 keV).

Table 4. Summary of the inefficiency measurement of the prototype strip. Only statistical errors were considered in the inefficiency values.

	Data	Simulation
N (total events)	7.6×10^5	1.04×10^8
N ($<$100 keV)	41	6318
Annihilation inefficiency	$(4.5 \pm 0.8) \times 10^{-5}$	$(4.0 \pm 0.06) \times 10^{-5}$
Photoelectron statistics inefficiency	$(0.9 \pm 0.3) \times 10^{-5}$	$(2.1 \pm 0.05) \times 10^{-5}$
Total inefficiency	$(5.4 \pm 0.8) \times 10^{-5}$	$(6.1 \pm 0.08) \times 10^{-5}$

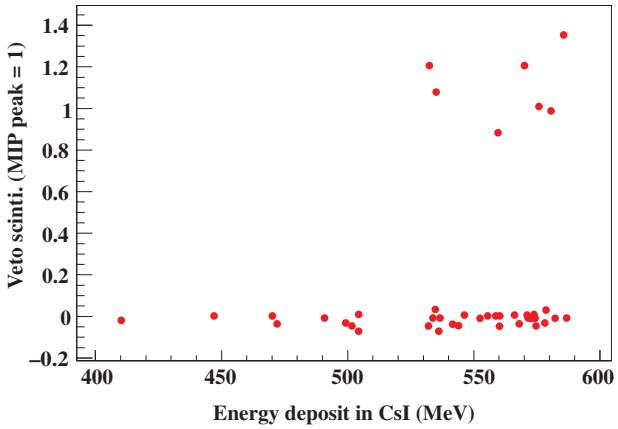

Fig. 9. Correlation between the energy deposits in the CsI counter and the veto scintillator. The energy deposit in the veto scintillator is normalized by the MIP peak value.

due to positron annihilation in the strip. The number of simulated inefficient events was calculated from the information on the particle that hit the prototype CV. In the simulation, 99% of the "photoelectron statistics" was due to the lower deposit energy under the grooves, and has the uncertainty due to the beam size, as mentioned before.[9] On the other hand, the "annihilation" had no influence from the beam profile. The resulting inefficiencies due to photoelectron statistics and annihilation

[9] In the simulation, such uncertainty was 50%.

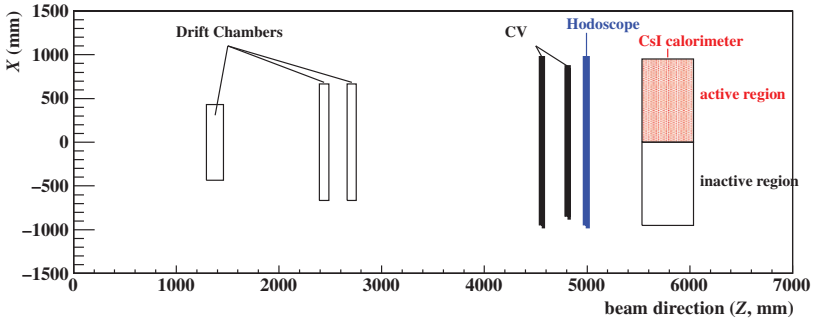

Fig. 10. Setup of the performance study at the KL beam line. Three sets of drift chambers were used to track charged particles, and a hodoscope placed downstream of the CV layers was used to trigger events.

were $(0.9 \pm 0.3) \times 10^{-5}$ and $(4.5 \pm 0.8) \times 10^{-5}$, respectively, and agreed with the MC within the error including the statistical error and the systematic effect of beam size. We concluded that we had a good understanding of the inefficiency in the positron detection.

4. Performance study at the beam line for the KOTO experiment

After completing the CV construction, we evaluated the performance of the CV at the neutral beam line for the KOTO experiment: the KL beam line in the J-PARC Hadron Experimental Facility (HEF). The measurement was carried out before the full installation of the KOTO detector. In this measurement, we evaluated the position dependence of the light yield, the timing resolution, and the inefficiency for charged particles that penetrate the CV layers. The charged particles were the particles from $K_L \to e^{\pm}\pi^{\mp}\nu$ decay, $K_L \to \mu^{\pm}\pi^{\mp}\nu$ decay, and $K_L \to \pi^+\pi^-\pi^0$ decay, and the mean momentum of these was 1 GeV/c. From the simulation, 59% of the charged particles were charged pions, 24% of these were muons, and 17% of these were electrons and positrons.

Figures 10 and 11 show a plan view of the experimental setup, and a rear view of the hodoscope and the calorimeter, respectively. The CV layers were located in front of the CsI calorimeter as in the case of the KOTO experiment.[10] The CsI calorimeter in the KOTO experiment consists of 2240 small and 476 large undoped CsI crystals. Their cross sections are 25 mm square and 50 mm square, respectively, and the length is 500 mm. Only half of the area of the calorimeter was available in this measurement, as shown in Fig. 11. A trigger hodoscope, which consisted of twelve 10 mm thick plastic scintillators, was installed between the CV and the CsI calorimeter. Three sets of drift chambers were placed upstream of the CV to track charged particles. Each set of the chambers measured the X and Y positions of the track separately. The pointing resolution of the chamber tracking at the CV layers was approximately 2 mm. The beam power of the J-PARC main ring accelerator for delivery to HEF was 6 kW at the time of this study. All counters in this study were located in air, while in the KOTO experiment most of the detectors, including the CV and the calorimeter, are operated in vacuum.

We required two hits in the hodoscope to collect events with two tracks penetrating the CV layers. In addition, at least one hit was required in each quadrant of the hodoscope that was included in a diagonal pair: the $(-X, +Y)$ and $(+X, -Y)$ or $(-X, -Y)$ and $(+X, +Y)$ regions. In the analysis, tracks were reconstructed with the hits in the chambers, and then a corresponding hit in the hodoscope was

[10] Distances from the calorimeter surface were slightly different in this study from those in the KOTO experiment.

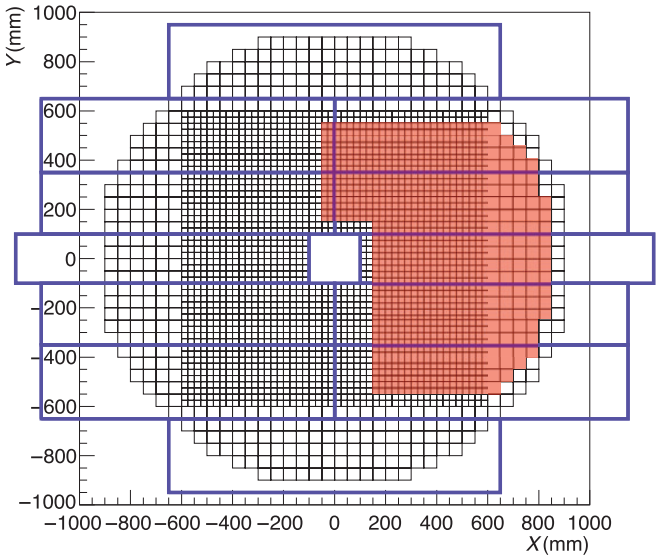

Fig. 11. Rear view of the trigger hodoscope and the calorimeter. Twelve scintillator plates, represented as rectangular boxes, covered the whole region of the CV and the calorimeter. The two sizes of squares in the array show the small and large CsI crystals in the calorimeter. In this study, only the region of the calorimeter shown in red was used for the inefficiency measurement.

required for each track to ensure that the particle penetrated the CV. Further information on the track was obtained by the fine-segmented CsI calorimeter. In the inefficiency measurement, the matching between the track extrapolation to the calorimeter and the hit location on the calorimeter was checked to eliminate the events in which a charged particle was scattered or decayed in flight. This limited the area for the inefficiency measurement to be about half of the total CV region, corresponding to the active area of the CsI calorimeter.

4.1. Evaluation of the light yield

We evaluated the light yield and determined that the CV satisfies our requirement: more than 10 p.e./100 keV in the entire area within the 850 mm radius. We first reconstructed two tracks through the chambers. From the measured X and Y positions, the tracks in the X–Z and Y–Z planes were reconstructed independently, where Z denotes the coordinate along the beam direction. To resolve the ambiguity of the combination of tracks, we required hits in the hodoscope corresponding to the combination.

The light yield of each CV strip was obtained as follows: we integrated a signal waveform, recorded by the 125 MHz ADC module, over the range of 64 samples (512 ns) and obtained the output charge. Next, we converted the output to the equivalent value in photoelectron units. The output charge for one photoelectron was derived for each MPPC from the charge distribution of dark noise, which was dominated by the thermoelectrons. We also made a correction for the path length in the strip. The output was scaled using the incident angle to the value in normal incidence.[11] We then summed the outputs from both ends of the strip and defined the sum as the light yield of the strip. To evaluate the light yield as a function of the track hit position, we used the average value in each

[11] Incident angles of charged particles in this study were less than 20°, and thus the correction was a few % in effect.

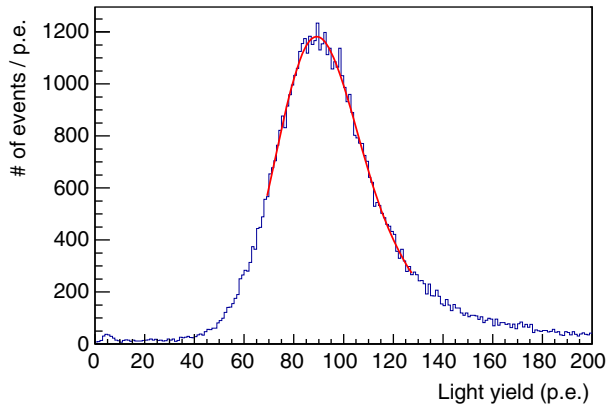

Fig. 12. Example of the light yield distribution of a CV strip. The histogram indicates the data, and the curve around the peak shows the fit corresponding to the convoluted function of Landau and Gaussian distributions. The events around 0 p.e. are due to scattering or decay in flight after the chambers.

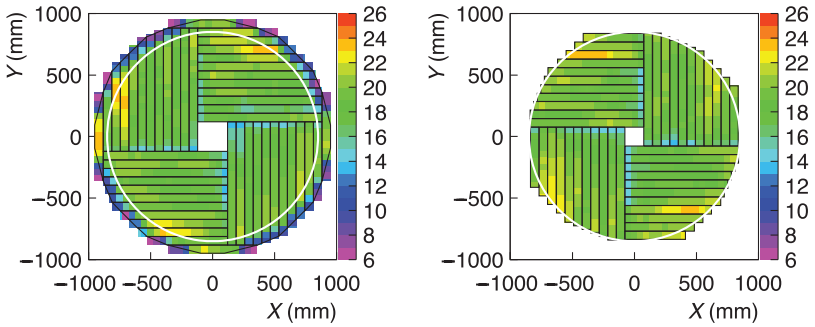

Fig. 13. Position dependence of the light yield. The left and right panels correspond to the results of the CV front and rear layers, respectively. Color indicates the light yield in units of p.e./100 keV, as shown in the legend. The white circle shows a radius of 850 mm. Smaller yields were observed at the ends of strips, which were due to smaller light collection in the regions where the fibers were not embedded in the scintillator (the outer ends of the strips in the rear layer do not have these regions of reduced light yield and thus no decreases were observed). Because the length of the WLS fibers for the long side at the outer strips is shorter than that at the inner strips due to the routing of the WLS fibers, the light yield in the outer region tends to be higher than that in the inner region. Higher light yields in some outer strips came from fluctuations in the scintillator thickness.

5 cm region in the longitudinal direction of the strip. Figure 12 shows an example of the light yield distribution. We applied a fit to the distribution, which was a convolution of Landau and Gaussian distributions. We defined the MIP peak as the most probable value in the resultant function. The corresponding energy deposit to the MIP peak was obtained by the simulation, and the light yield value was normalized by energy deposit in units of p.e./100 keV. Figure 13 shows the position dependence of the light yield. The light yield exceeded 10 p.e./100 keV in the whole region within a 850 mm radius, and the average value over the region was 18.6 p.e./100 keV.

4.2. Evaluation of the timing resolution

We evaluated the timing resolution and determined that the CV satisfies our requirement: better than 3 ns for the entire area within the 850 mm radius. Similar to the light yield study, we obtained the results for tracks in each 5 cm region in the longitudinal direction of the strip. The hit timing at each end was calculated by using a constant fraction method; from a waveform recorded in the 125 MHz

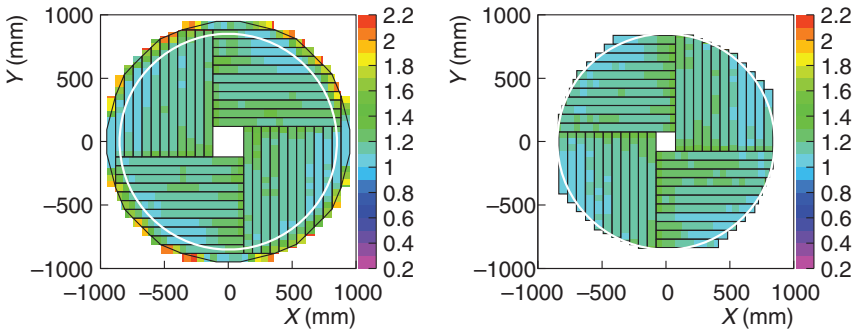

Fig. 14. Position dependence of the timing resolution (σ_{Mean}). The left and right panels correspond to the results of the CV front and rear layers, respectively. Color indicates the timing resolution in units of ns, as shown in the legend.

ADC module, gaps between neighboring samples were interpolated by a linear function, and the time where the signal height reached the half of the maximum height in the leading edge was determined. In this study, we used the difference in the hit timings at both ends in order to eliminate the fluctuation due to a timing resolution of the trigger hodoscope, while the hit timing in the KOTO experiment is defined as the mean of hit timings at both ends. In an ideal case, the mean time and the time difference satisfy the equation:

$$\sigma_{\mathrm{Mean}} = \frac{\sigma_{\mathrm{Difference}}}{2} = \frac{\sqrt{\sigma^2_{\mathrm{Short}} + \sigma^2_{\mathrm{Long}}}}{2}, \tag{1}$$

where σ_{Mean}, $\sigma_{\mathrm{Difference}}$, σ_{Short}, and σ_{Long} show the root-mean-square of the distributions of the mean time, the time difference, and the hit times at both ends (short and long sides), respectively. We calculated the expected timing resolution in the KOTO experiment (σ_{Mean}) by dividing $\sigma_{\mathrm{Difference}}$ by two.[12] Figure 14 shows the position dependence of the timing resolution. Comparing it with Fig. 13, the timing resolution is larger in the region where the light yield was small. This is due to the fact that a smaller light yield caused a larger time jitter of the signal pulse.

The timing resolution is less than 3 ns in the entire region within the 850 mm radius, and the average timing resolution over the region is 1.2 ns.

4.3. Evaluation of the inefficiency

The analysis of the inefficiency consisted of four steps: 1) event topology selection, 2) candidate track selection, 3) CV hit decision, and 4) correction.

4.3.1. Event topology selection

First, tracks were found using the drift chambers. Then a corresponding hit in the trigger hodoscope was required for each of the two candidates, as described in Sect. 4. Events were further required to have a topology with one track going into the CsI active region ("near-track") and the other into the opposite side ("far-track"). To ensure the correct combination of tracks in the X–Z and Y–Z planes, the far-track needs to have corresponding hits in the CV strips. Only the near-tracks were used to measure the inefficiency.

[12] The time difference depends on the hit position since the propagation times to both ends change; the resolution here included this contribution. The contribution to σ_{Mean} in the case of a 5 cm region was estimated to be 0.1 ns and was disregarded in this study.

4.3.2. Candidate track selection

The second step selected candidate "near-tracks" that ensured penetration into the CV. Our major concern was charged particles that decay in flight or scatter in the materials between the chamber and the CV, so that they actually miss the strip that was pointed to by the reconstructed track. These "non-penetrating" tracks could fake inefficient events, and were removed by applying the following cuts. First, a CsI hit was requested at the position that matched the track (track–CsI matching cut). The distance ΔR, between the position of the CsI hit and the chamber tracks, had to be $\Delta R < 30\,\mathrm{mm}$.[13] The CsI hit position was defined as the center of energy deposits in the crystals that formed a cluster around the particle's incident position. Since the active area of CsI was smaller than that of the CV, the track–CsI matching cut restricted, in effect, the track position to be within a 720 mm in radius (outer fiducial cut). Second, tracks were rejected when the expected position at the CV was closer than 200 mm from the beam center (inner fiducial cut). This cut was useful to remove those particles that decayed or scattered into the beam hole.[14] These cuts described above were found to remove non-penetrating tracks almost entirely.

4.3.3. CV hit decision

The third step selected hits in the CV. Given a near-track that passed the cuts in the second step, we examined those CV strips that had an overlap with a virtual square set on the CV plane whose center was placed at the track's expected position. The size of the square was chosen to be 14 cm × 14 cm considering the width of the CV strips, and the number of examined strips was 2 to 5, depending on the track position. We then took the maximum energy deposit among these strips as the CV energy deposit for the track under consideration. To check the validity of each selection, we carried out an MC simulation that took into account the response of the detectors (the chambers, CV, hodoscope, CsI, in-beam material). We simulated the three main decay modes: $K_L \to e^{\pm}\pi^{\mp}\nu$, $K_L \to \mu^{\pm}\pi^{\mp}\nu$, and $K_L \to \pi^+\pi^-\pi^0$. Figure 15 shows the energy distribution of data and simulation determined by this method. The agreement between data and simulation was good. The simulation was also used for correcting the inefficiency, as mentioned later. The CV is defined to have a hit if it has an energy deposit more than 100 keV, and CV inefficiency was defined as the fraction of tracks that had no hits. We denote this inefficiency by I_{raw}. In the data, the inefficiencies were $I^{\mathrm{data}}_{\mathrm{raw(f)}} = (1.13 \pm 0.24) \times 10^{-5}$ and $I^{\mathrm{data}}_{\mathrm{raw(r)}} = (1.43 \pm 0.26) \times 10^{-5}$, respectively. The errors indicate statistical uncertainties. In the simulation, the estimated inefficiencies were $I^{\mathrm{MC}}_{\mathrm{raw(f)}} = (1.36 \pm 0.16) \times 10^{-5}$ and $I^{\mathrm{MC}}_{\mathrm{raw(r)}} = (1.64 \pm 0.18) \times 10^{-5}$, respectively. The uncertainty is the statistical error. The inefficiency of data and MC agreed well.

4.3.4. Correction

The fourth step is a correction to I_{raw}, obtained above. There are two main factors that should be taken into account: one related to non-penetrating tracks and the other related to accidental hits. The former would cause the measured inefficiency (I_{raw}) to be larger than the true value, while the latter would cause it to be smaller. We consider them in turn below. As described above, non-penetrating tacks were removed almost entirely by the track–CsI matching cut. Some non-penetrating

[13] This cut value, 30 mm, was chosen considering the resolution of ΔR ($\sim$16 mm), which was mainly due to the position resolution of the calorimeter to the charged particles.

[14] Intuitively, this could be understood as the sum of ΔR (30 mm) and half of the size of the maximum length of the beam hole (diagonal direction $\sim$170 mm).

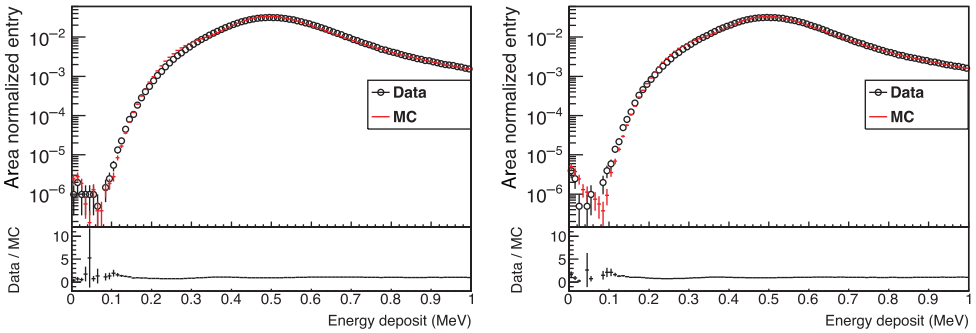

Fig. 15. Energy deposit distribution of the CV layers after applying all the cuts. The left and right panels correspond to the results of the front and rear layers, respectively. The dots show the data and the histogram shows simulation results. These spectra were normalized in the same way as in Fig. 8. The small discrepancy in the region around 300 keV was considered to be due to the reproducibility of the response in the region where the WLS fibers were embedded. In addition, the discrepancy in the region lower than 150 keV was considered to be due to the reproducibility at the boundary of the scintillator. The light collection at the boundary is smaller.

tracks, however, survived the cut; for instance, the events that underwent the $K_L \to \pi^+\pi^-\pi^0$ decay upstream of the CV could fake "correct" CsI hits with the photon(s) from π^0. Another example is tracks that scattered, producing Bremsstrahlung photon(s). We relied on MC simulation to estimate the contribution of these residual non-penetrating tracks, which made the apparent CV inefficiency larger. We will correct the raw inefficiency later (Eq. 2), introducing a variable $C_{\text{n.p.}}$, which is the ratio of non-penetrating tracks to all the tracks in the final selection. Figure 16(a) shows the distribution of ΔR for the tracks that passed all the cuts in the three steps described above, except for ΔR. The data and simulation agree within 18%. We note that, in the simulation, non-penetrating tracks could be identified unambiguously (see the histogram in green). Figure 16(b) shows a ΔR distribution for the inefficient tracks with CV energy deposits of less than 100 keV. An important observation in this figure is that some non-penetrating tracks (shown in green) satisfied the $\Delta R < 30$ mm cut. Among the 73 (88) inefficient tracks in the front (rear) layer with $\Delta R < 30$ mm, 27 (42) tracks were identified as being from non-penetrating tracks. $C_{\text{n.p.}}$ is $0.37^{+0.19}_{-0.21}$ for the front layer, and $0.48^{+0.18}_{-0.19}$ for the rear layer. The errors came mainly from three sources: the first one from statistical uncertainty of MC (± 0.08 or ± 0.09), the second from the cutout size in the MC, which could affect the ratio through the number of inefficient events for penetrating tracks $\left(^{+0.09}_{-0.07}\text{ or }^{+0.10}_{-0.07}\right)$,[15] and the last one from possible modeling errors on penetrating and/or non-penetrating tracks by MC, which was evaluated with separate control samples (± 0.15 or ± 0.16).[16]

Next, we considered the effects caused by accidental hits. According to the data, the mean multiplicity of the CV hits among the strips defined by the 14 cm $\times$ 14 cm squares was 1.044 for the front layer and 1.052 for the rear layer. The probability of the extra activity, $\sim$0.05, is a rough measure of the correction factor for accidentals. We elaborated this estimate with the help of MC studies; i.e., we overlaid MC events with real accidental data taken with a random trigger whose rate is proportional to the instantaneous rate, and studied the nature of accidental hits and the rate. In addition to the real

[15] Machining error of the cutouts was taken into account, when $C_{\text{n.p.}}$ was calculated in the MC.

[16] We prepared two kinds of control samples, penetrating enriched and non-penetrating enriched samples, by applying additional cuts for both data and MC. Any modeling errors should appear as discrepancies between MC and data more clearly for those samples. We found that they agreed well with each other within statistics, and put possible deviations as systematic uncertainties.

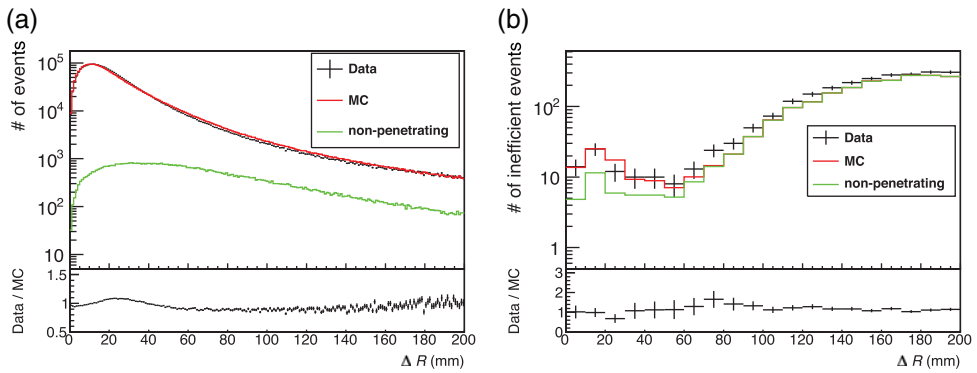

Fig. 16. (a) Distribution of "near-tracks" as a function of ΔR. (b) Distribution as a function of ΔR of the tracks that had energy deposits of less than 100 keV at the front layer or rear layer. The histogram labeled "non-penetrating" shows the events in which an uncharged particle hit the corresponding CV strip, according to the true information obtained from the simulation. The histogram for the simulation was normalized to the number of measured "near-tracks" for (a) and inefficient events for (b), respectively.

accidental hits, stemming from uncorrelated particles in the beam, we found that there are correlated activities caused by, e.g., a delta ray and/or a backsplash from the CsI calorimeter. The probability of the accidental CV hits $\left(C_{\mathrm{acc}}\right)$ that contribute to the efficiency calculation was found to be slightly smaller than the mean hit multiplicity: the values are $C_{\mathrm{acc(f)}} = 0.031 \pm 0.006$ for the front layer and $C_{\mathrm{acc(r)}} = 0.043 \pm 0.006$ for the rear layer. The errors came mainly from systematic uncertainties, which were evaluated from discrepancies in the CV hit distributions between the data and MC with accidental overlay.

4.3.5. Results of inefficiency measurements

The raw inefficiency was corrected by the equation

$$I_{\mathrm{corr}} = I_{\mathrm{raw}} \times \left(1 - C_{\mathrm{n.p.}}\right) \times \left(\frac{1}{1 - C_{\mathrm{acc}}}\right). \tag{2}$$

The results were $I_{\mathrm{corr(f)}} = \left(0.74 \pm 0.15^{+0.25}_{-0.22}\right) \times 10^{-5}$ and $I_{\mathrm{corr(r)}} = \left(0.77 \pm 0.14^{+0.28}_{-0.27}\right) \times 10^{-5}$, for the front and rear layers, respectively, where the first errors are statistical and the second errors are systematic. The source of the systematic errors is dominated by those from $C_{\mathrm{n.p.}}$ and C_{acc}; other sources, such as the stability of the energy deposit and the deviation of each cut, were small and were thus neglected.

We investigated the hit position of the inefficient tracks on the CV. As shown in Fig. 17, the majority of the inefficient points were found to be located near the cutouts or on the edges of the scintillator strips, and not in the central region. This may be regarded as evidence that the CV was built as designed. Finally, we set the upper limit of the inefficiency from I_{corr}. Assuming Poisson statistics, the upper limit was found to be 1.5×10^{-5} (90% CL) and 1.5×10^{-5} (90% CL) for the front and rear layers, respectively. We conclude that the CV achieved a high efficiency $\left(<1.5 \times 10^{-5}\right.$ of inefficiency$\left.\right)$ and satisfied the requirements for the KOTO experiment.

5. Conclusion

We have developed a low-mass and high-efficiency charged-particle detector for the KOTO experiment at J-PARC. Two layers of 3 mm thick plastic scintillators with embedded wavelength-shifting fibers, each of which was read by MPPCs, were manufactured. The MPPC, which has 3 mm × 3 mm

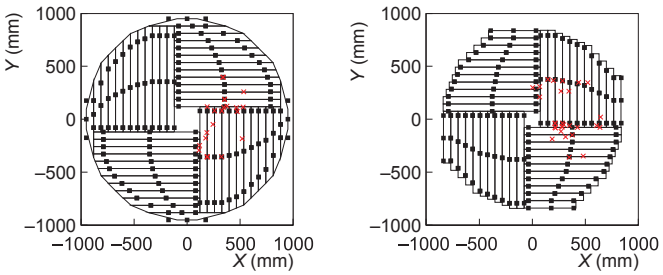

Fig. 17. Hit positions of the inefficiency tracks in the CV layers. The left and right panels show the front and rear layers, respectively. The crosses show the positions calculated by the chamber tracking. The squares on the edges of the strips indicate the position of the cutouts used to hold the scintillator strips in place. The sizes of the cutouts are magnified 50 times in the plot.

sensitive area and is equipped with a thermoelectric cooler, was newly developed for this purpose. After completing the construction, performance studies were conducted at the neutral kaon beam line for the KOTO experiment in the J-PARC Hadron Experimental Facility. We measured the light yield, the timing resolution, and the inefficiency against penetrating charged particles. The resultant light yield per 100 keV energy deposit was 18.6 p.e. on average, and the timing resolution of the scintillator strips was measured to be 1.2 ns. In particular, the detection inefficiency against the particles that penetrated the CV, per layer, was less than 1.5×10^{-5} over the area within a radius of 850 mm.

Acknowledgements

We are grateful to the staff members of the KEK for their cooperation in the construction of the CV and the measurement of its performance. We also thank the staff members of the ELPH accelerator, J-PARC accelerator, Hadron Beam groups, and the KEK Computing Research Center for their support in taking and analyzing the physics data. Part of this work was supported by JSPS/MEXT KAKENHI Grant Numbers 23224007 and 8071006. Some of the authors were supported by a Grant-in-Aid for JSPS Fellows.

References

[1] J. Brod, M. Gorbahn, and E. Stamou, Phys. Rev. D **83**, 034030 (2011).
[2] M. Blanke, PoS **KAON13**, 010 (2013).
[3] J. K. Ahn et al. [E391a Collaboration], Phys. Rev. D **81**, 072004 (2010).
[4] T. Yamanaka [KOTO Collaboration], Prog. Theor. Exp. Phys. **2012**, 02B006 (2012).
[5] *Japan Proton Accelerator Research Complex* (Available at: http://j-parc.jp, date last accessed: March 6, 2015).
[6] Hamamatsu Photonics catalog, Cat. No. KAPD0002J05 (August 2009).
[7] *Saint-Gobain* (Available at: http://www.crystals.saint-gobain.com, date last accessed: March 6, 2015).
[8] *Kuraray Co., Ltd.* (Available at: http://www.kuraray.co.jp/en/, date last accessed: March 6, 2015).
[9] *Hamamatsu Photonics K. K.* (Available at: http://www.hamamatsu.com/jp/en/index.html, date last accessed: March 6, 2015).
[10] *Oike & Co., Ltd.* (Available at: http://www.oike-kogyo.co.jp/english/index.html, date last accessed: March 6, 2015).
[11] *Eljen Technology* (Available at: http://www.eljentechnology.com/index.php, date last accessed: March 6, 2015).
[12] M. Bogdan et al., Nuclear Science Symp. Conf. Record, NSS '07, Vol. 1, pp. 133–134 (2007).
[13] M. Bogdan et al., 16th IEEE-NPSS Real Time Conf., RT '09, pp. 443–445 (2009).